# Beam-dynamics driven design of the LHeC energy-recovery linac

Dario Pellegrini,* Andrea Latina, and Daniel Schulte
*CERN, Geneva CH-1211, Switzerland*

S. Alex Bogacz
*Jefferson Lab, Newport News, Virginia 23606, USA*
(Received 3 September 2015; published 23 December 2015)

The LHeC is envisioned as a natural upgrade of the LHC that aims at delivering an electron beam for collisions with the existing hadronic beams. The current baseline design for the electron facility consists of a multipass superconducting energy-recovery linac (ERL) operating in a continuous wave mode. The unprecedently high energy of the multipass ERL combined with a stringent emittance dilution budget poses new challenges for the beam optics. Here, we investigate the performances of a novel arc architecture based on a flexible momentum compaction lattice that mitigates the effects of synchrotron radiation while containing the bunch lengthening. Extensive beam-dynamics investigations have been performed with PLACET2, a recently developed tracking code for recirculating machines. They include the first end-to-end tracking and a simulation of the machine operation with a continuous beam. This paper briefly describes the Conceptual Design Report lattice, with an emphasis on possible and proposed improvements that emerged from the beam-dynamics studies. The detector bypass section has been integrated in the lattice, and its design choices are presented here. The stable operation of the ERL with a current up to ∼150 mA in the linacs has been validated in the presence of single- and multibunch wakefields, synchrotron radiation, and beam-beam effects.

DOI: 10.1103/PhysRevSTAB.18.121004 PACS numbers: 41.75.Fr

## I. INTRODUCTION

Two of the initially proposed options for the LHeC, the Linac Ring and the Ring Ring, both offered comparable performances. However, the Linac Ring has recently been selected as the baseline; the choice was mainly based on minimizing interference with the LHC operation. A PLACET2 [1] simulation has been set up to validate the energy-recovery linac (ERL) performance. The beam-dynamics studies pointed out a number of possible improvements of the ERL design which will be discussed in this paper. Moreover, the initial lattice presented in the Conceptual Design Report (CDR) has been augmented with the detector bypass, an essential step towards the completion of this design.

The ERL design for the LHeC electron facility is sketched in Fig. 1. The racetrack layout hosts two superconducting linacs in the parallel straights and three recirculating arcs on each side. Its total length is 9 km, 1/3 of the LHC circumference. An integer fraction is required to guarantee that, in the presence of an ion-cleaning gap in the electron beam, the proton bunches collide with electrons either always or never.

Each of the two linacs is about 1 km long and provides a total acceleration of 10 GeV. The injection energy has been chosen at 500 MeV. In order to reach the collision energy of 60 GeV, the electrons are recirculated three times. Beams of different energies are directed into different recirculation arcs via beam spreaders or recombiners, which introduce or remove vertical separation at each end of the linacs. All the arcs share the same radius of 1 km and are staked vertically in the same tunnel. In addition, arc2 and arc4 are equipped with bypasses to avoid interference with the detector.

After the collision with the LHC proton or ion beam, the electron beam is decelerated in three subsequent turns. Its energy is released into the rf and used to accelerate the fresh beam. This allows one to increase the beam current and

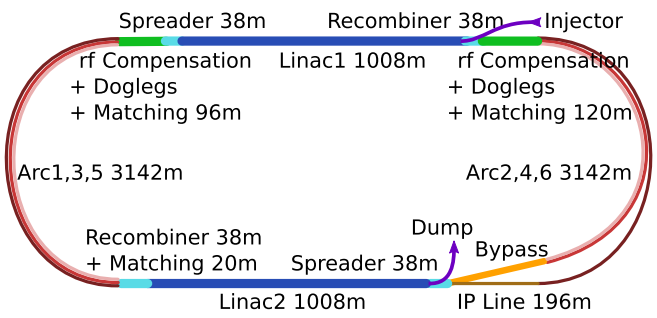


FIG. 1. Scheme of the LHeC electron facility.

*Also at EPFL, Lausanne CH-1015, Switzerland.

TABLE I. Fundamental beam parameters of the baseline and Higgs factory LHeC.

| | Baseline | | Higgs factory | |
|---|---|---|---|---|
| | $e^-$ | $p$ | $e^-$ | $p$ |
| Beam energy [GeV] | 60 | 7000 | 60 | 7000 |
| Bunch spacing [ns] | 25 (50) | 25 (50) | 25 (50) | 25 (50) |
| Bunch intensity (nucleons) [$1 \times 10^{10}$] | 0.1 (0.2) | 17 | 0.4 (0.8) | 22 (35) |
| Beam current [mA] | 6.4 | 860 | 25.6 | 1110 (883) |
| rms bunch length [mm] | 0.6 | 75.5 | 0.6 | 75.5 |
| Normalized rms emittance [$\mu$m] | 50 | 3.75 | 50 | 2.5 (3.0) |
| IP beta function $\beta^*_{x,y}$ [m] | 0.12 | 0.1 | 0.039 | 0.05 |
| IP spot size [$\mu$m] | 7.2 | 7.2 | 4.1 | 4.1 |
| Hadron beam-beam parameter | $1 \times 10^{-4}$ $(2 \times 10^{-4})$ | | $4 \times 10^{-4}$ $(8 \times 10^{-4})$ | |
| Lepton disruption parameter $D$ | 6 | | 23 (31) | |
| Crossing angle | 0 | | 0 | |
| Hourglass reduction factor | 0.91 | | 0.70 (0.73) | |
| Pinch enhancement factor | 1.35 | | 1.35 | |
| Center of mass energy [GeV] | 1300 | | 1300 | |
| Luminosity [$1 \times 10^{33}$ cm$^{-2}$ s$^{-1}$] | 1.3 | | 16 (22) | |

luminosity while limiting the power consumption [2]. The machine is intended to operate continuously, and bunches of different passes will interleave in the linacs. The ultimate beam parameters have recently been revised to reach a luminosity $>1 \times 10^{34}$ cm$^{-2}$ s$^{-1}$; they are presented in Table I. Such a high luminosity, 250 times the one previously achieved at HERA [3], allows one to employ the LHeC as a Higgs factory [4]. All the studies presented in this paper are based on the ultimate set of parameters. It should be noted that the initial stage may use more conservative parameters, in particular, a factor of 4 smaller beam current.

## II. LATTICE COMPONENTS

### A. Linacs

The two 1 km long linacs consist of 18 FODO cells each. Following each quadrupole, two cryomodules are placed, each containing eight cavities operating at 802 MHz, for a total of 576 cavities per linac.

When moving to the next linac, the $\beta$ functions must be preserved, with the only exception the sign of their derivatives. This comes from the fact that, when decelerating, the beam keeps turning in the same direction; therefore, any possible arc matching aiming at optimizing the Twiss functions at each linac injection during the acceleration would cause a mismatch during the deceleration.

The optics of the two linacs are symmetric, the first being matched to the first accelerating passage and the second to the last decelerating one. We assumed a parabolic profile (three degrees of freedom) for the quadrupolar strengths along the linacs. The strength profile has been optimized together with the initial beta function and its derivative in order to minimize the impact of imperfections and collective effects such as wakefields, driven by the parameter

$$\left\langle \frac{\beta}{E} \right\rangle = \int_{\text{Acceleration}} \frac{\beta}{E} ds.$$

When optimizing for long-range wakefields, one could also consider the interaction of bunches at different turns. This results in the integrals

$$I_{ij} = \int_{\text{Linac1,2}} \frac{\sqrt{\beta_i \beta_j}}{\sqrt{E_i E_j}} ds,$$

where $E$ is the beam energy, $\beta$ is the lattice function, and $i, j$ indicate the turn number. The merit function (for the acceleration only) then becomes

$$F = \sqrt{(I_{11} + I_{22} + I_{33})^2 + 2(I_{12} + I_{23})^2 + 2(I_{13})^2}.$$

The solution obtained minimizing $F$ is almost identical to the one that considers only the trace of $I$.

The second-order term in the quadrupolar strength profile becomes extremely small and improves the total integral only by 1%; therefore, we discarded it, assuming a linear profile. The result of this optimization is not far from the 130° FODO lattice which we have initially designed (see Fig. 2) and already matched to the arcs. For this reason, we used that design for our investigation of the beam dynamics.

Substantial improvements have been obtained placing a quadrupole after every cryomodule instead of every two, as shown in Fig. 3. In this case, the merit function is almost halved. As most of the contribution to the merit function comes from the very low energies, the additional quadrupoles may be inserted only in the initial (final) part of linac1 (linac2). This may be considered as a possible upgrade to improve the stability of the highest beam currents of the Higgs factory.

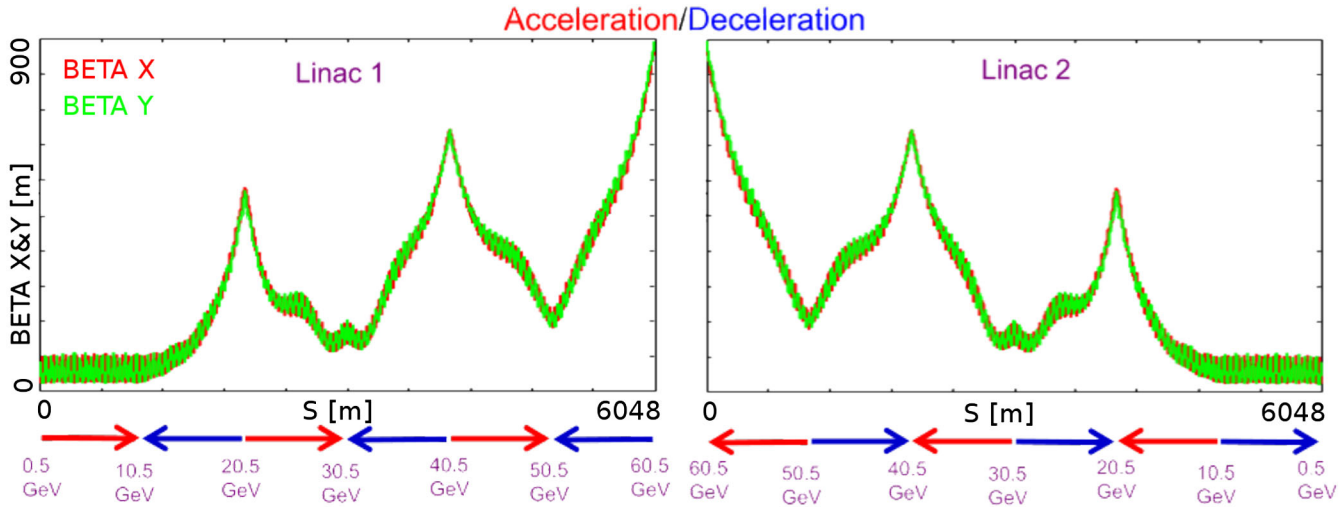


FIG. 2. Optics functions in the linacs for the subsequent passages. The red (blue) arrows indicate the accelerating (decelerating) passages.

### B. Arcs

To accomplish the multiturn recirculation, six arcs are accommodated in a tunnel of 1 km radius. The lattice cell adopts a flexible momentum compaction layout that presents the very same footprint for each arc. This allows us to stack magnets on top of each other or to combine them in a single design [5]. The dipole filling factor of the cell is 76%; therefore, the effective bending radius is 760 m.

The tuning of each arc takes into account the impact of synchrotron radiation at different energies. At the highest energy, it is crucial to minimize the emittance dilution; therefore, the cells are tuned to minimize the dispersion in the bending sections, as in a theoretical minimum emittance lattice. At the lowest energy, it is possible to compensate for the bunch elongation with a negative momentum compaction setup which, additionally, contains the beam size.

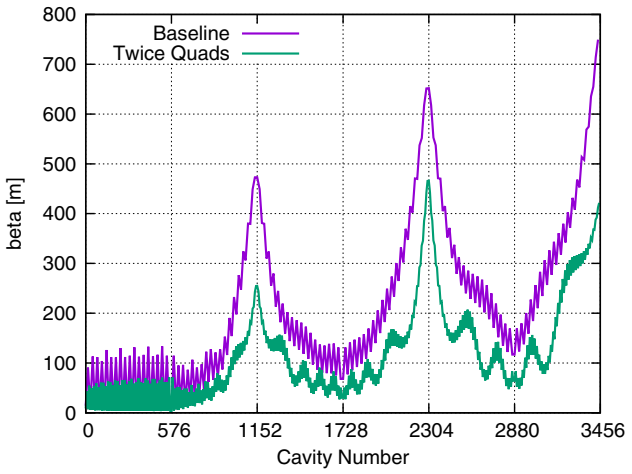


FIG. 3. Evolution of the $\beta$ function during the acceleration in the newly optimized linacs. The baseline lattice with a quadrupole every two cryomodules is compared to a proposal with twice the number of quadrupoles.

The intermediate energy arcs are tuned to a double bend achromat (DBA)-like lattice, offering a compromise between isochronicity and emittance dilution. Figure 4 illustrates all three settings of the arc cells.

The strengths of the magnets along the arcs slightly decrease according to the energy lost by radiation. The energy lost due to synchrotron radiation has to be replenished back to the beam, so that at the entrance of each arc the accelerating and decelerating beams have the same energy. As shown in Fig. 5, they employ the second-harmonic rf frequency, so that each section can restore the energy lost in the corresponding arc for both the accelerating and the decelerating beams. Table II shows the energy loss for each arc and the corresponding power (all the arcs transport a 50 mA current, except for arc6 which sees only 25 mA). The required number of cryomodules assumes the parameters shown in Table III. They have been extrapolated from the ILC cavity design, expecting that the higher frequency and lower gradient would support continuous operation.

The compensating cavities are placed into the linac1 side of the racetrack, before the bending section of arc1, arc3, and arc5 and after the bending section of arc2, arc4, and arc6. This saves space on the linac2 side to better fit the interaction point (IP) line and the bypasses. Note that with the current vertical separation of 0.5 m it will not be possible to stack the cryomodules on top of each other; therefore, they will occupy 42 m on the arc4 and arc6 side and 24 m on the arc3 and arc5 side of the racetrack.

The heat load from synchrotron radiation is 6 kW/m for both arc6 and arc5; the latter is at lower energy, but it transports twice the amount of current. This is a factor of 3.5 higher with respect to LEP II, where the vacuum chamber was kept below 50 °C with 79 m long cooling circuits. As reported in Ref. [6], shorter cooling circuits allow one to dissipate more power and could be adapted for the LHeC case.

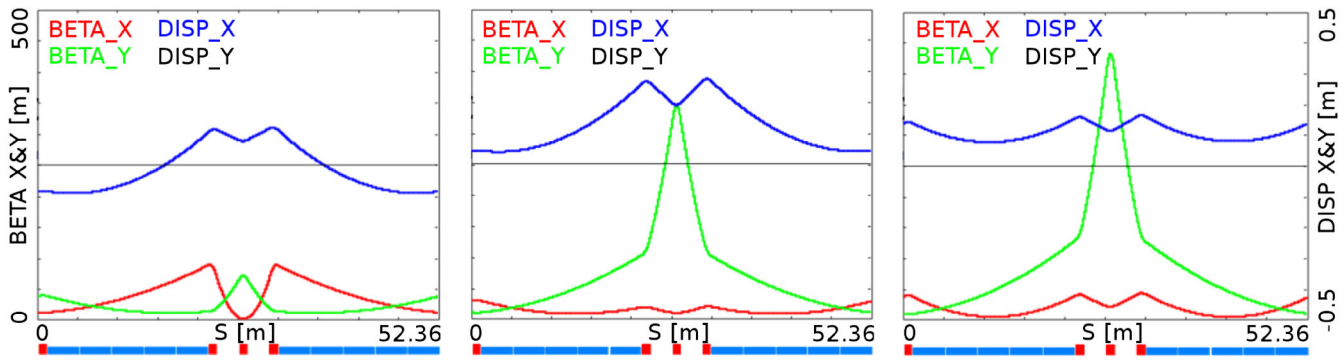


FIG. 4. Lattice cells of arc1 and arc2 (left), arc3 and arc4 (center), and arc5 and arc6 (right).

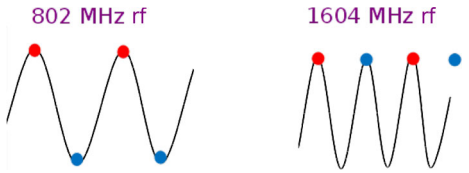


FIG. 5. The second-harmonic rf restores the energy loss in both the accelerating and decelerating passages.

Each of the compensating cavities in arc5 needs to transfer up to 1 MW to the beam. Although a 1 MW continuous wave klystron is already operating at the BNL ERL [7], the cryomodule integration and protection system will require a careful design.

The impact of the energy-independent coherent synchrotron radiation (CSR) have been estimated with the analytical formula derived in Ref. [8]. Each arc causes an energy loss of 1 MeV and introduces an energy spread of $7 \times 10^{-5}$. The CSR has not been included in tracking simulations as it is not expected to be the dominant effect.

An alternative design based on combined function magnets is also being investigated. Preliminary studies showed promising results.

### C. Spreader and recombiner

The spreaders are placed after each linac, and they separate the bunches at different energies in order to route them to the corresponding arcs. The recombiners do just the opposite, merging the beams into the same trajectory before entering the next linac.

The spreader design consists of a vertical bending magnet, common for all beams, that initiates the separation. The highest energy, at the bottom, is brought back to the horizontal plane with a chicane. The lower energies are captured with a two-step vertical bending. This two-step design simplifies the suppression of vertical dispersion; however, it induces a non-negligible energy loss, especially for arc4, and also it drives the horizontal $\beta$ function to very high values.

A new single-step design developed for arc2 and arc4 targets both drawbacks. It employs seven quadrupoles to control the dispersion between the two bending dipoles. The energy loss is reduced by factor of 5, and at the same time both the dispersion and the $\beta$ functions are mitigated. To avoid magnet interference, the quadrupoles of the two beam lines were appropriately shifted longitudinally. The final integrability of the systems still needs to be verified with technical drawings. The maximum quadrupole gradient of 80 T/m cannot be reached with warm magnets, although it is not too challenging to adopt superconducting technology, since the cryogenics is readily available from the nearby linacs.

A comparison of the two designs for the arc2 spreader is shown in Fig. 6. Both of them provide a final vertical separation of ~0.5 m between the three arcs.

TABLE II. Energy loss, power dissipation, and the required number of compensating cryomodules for each arc.

| Arc | $E$ [GeV] | $\Delta E$ [MeV] | $P$ [MW] | Cryomodules |
|---|---|---|---|---|
| 1 | 10.4 | 0.7 | 0.04 | 0 |
| 2 | 20.3 | 9.9 | 0.5 | 0 |
| 3 | 30.3 | 48.5 | 2.4 | 1 |
| 4 | 40.2 | 151 | 7.6 | 1 |
| 5 | 50.1 | 365 | 18.2 | 3 |
| 6 | 60.0 | 751 | 18.8 | 6 |
| Total | | 1901 | 47.5 | 10 |

TABLE III. A tentative parameter list for the compensating rf cryomodules extrapolated from the ILC design.

| | |
|---|---|
| Frequency | 1604 MHz |
| Gradient | 30 MV/m |
| Design | Nine cells |
| Cells length | 841 mm |
| Structure length | <1 m |
| Cavity per cryomodule | 6 |
| Cryomodule length | ~6 m |
| Cryomodule voltage | 150 MV |

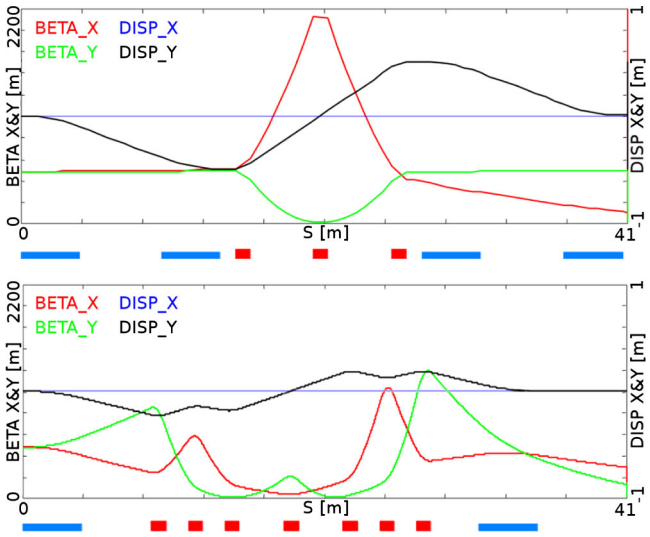


FIG. 6. Optics functions for the two-step vertical spreader (top) compared with the new design of a single-step spreader (bottom). Both plots refer to arc2, the arc4 design being very similar. The scales are equal for both plots.

### D. Bypasses

Recent studies explored the possibility to install the LHeC detector inside the magnet originally built for the L3 experiment at LEP and now being employed by the ALICE experiment at the LHC. The outer radius of this magnet is 7.9 m [9]. The vertical separation provided by the spreader (see Sec. II C) is not sufficient for the 20 and 40 GeV beams to avoid the detector; therefore, one needs to design bypasses. The minimization of the bending of the beam is crucial to mitigate the effects of synchrotron radiation. The bypasses are placed at the beginning of arc2 and arc4, and they displace the two beams by 10 m with respect to the IP. The separation takes place in the horizontal plain, towards the inside of the racetrack, as illustrated in Figs. 1 and 7.

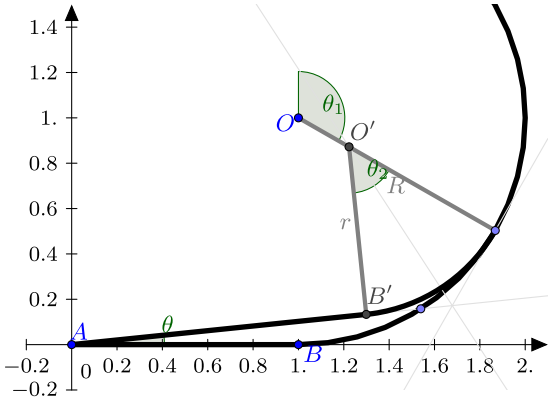


FIG. 7. Scheme of the bypass geometry. The IP line $\overline{AB}$ has been purposely stretched, being actually ∼1/5 of the arc radius.

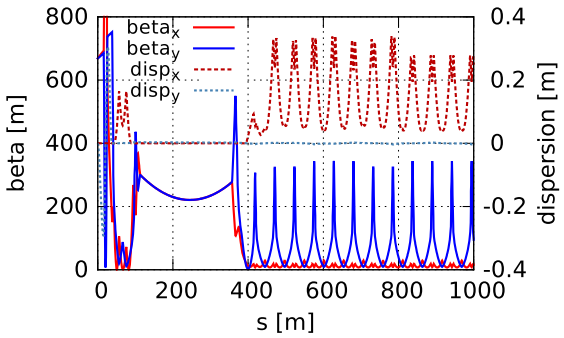


FIG. 8. Beta functions and dispersion at the beginning of arc4 with the detector bypass included. It features the vertical spreader, the initial horizontal bending, the straight section, the modified dispersion suppressor, seven junction cells, and four regular cells.

Ten arclike dipoles were placed very close to the spreader, to provide an initial bending, which results in 10 m separation from the detector located 150 m downstream. The straight section of the bypass is approximately 300 m long. Its magnet-free design may be helpful to minimize the separation from the detector. Furthermore, it may be utilized for beam diagnostics and path length adjustment. In order to joint the footprint of arc6, ten of the 60 standard cells in arc2 and arc4 are replaced with seven higher field cells. The number of junction cells is a compromise between the field strength increase and the length of additional bypass tunnel, as can be inferred from Fig. 7.

Figure 8 shows the Twiss functions at the beginning of arc4. The quadrupole strengths in the junction cells are the same as in the arc cells. This creates a slight mismatch in the junction cells that is removed in the dispersion suppressor. In arc2, the mismatch is more evident, and it has been corrected by adjusting the quadrupoles in the last junction cell and in the first regular cell.

## III. TRACKING SIMULATIONS

The two linacs and the six arcs, properly connected together, have been imported in PLACET2 [10]. This code implements the recirculation in a realistic way. Each element is defined only once, and its phase is computed with respect to the beam time of flight. Moreover, it allows one to simultaneously track multiple bunches preserving their time sequence everywhere in the machine. The beam-beam effect is computed by GUINEA-PIG [11].

For all the subsequent studies, the beam parameters used are those of the Higgs factory, listed in Table I.

The two-step design of the spreader and recombiner sections was used, neglecting the radiation in these sections, as it proved to be unrealistically high. The second-harmonic rf, required to replenish the energy lost by synchrotron radiation, is currently modeled as a thin element. The final focus system and the postcollision line are transfer matrices.

### A. Single-bunch tracking

The single-bunch tracking allows one to verify the beam transport. Figure 9 shows the Twiss parameters obtained following a bunch along its path throughout the whole machine. The linacs are easily identifiable by looking at the energy profile. In the arcs, the energy stays almost constant, the only variation being caused by the synchrotron radiation. One can notice the different average values of the $\beta$ functions in different arcs, as described in Sec. II B. A small beta beating can be barely noted in the arcs, being a result of using a different model of the rf focusing in the linacs between PLACET2 and OPTIM (the program used for the optics matching).

During the transport, the main degrading effects on the bunch quality are the incoherent synchrotron radiation and short-range wakefields; both are implemented in PLACET2. An approximation of the wake functions has been computed using the formulas from Ref. [12] and the cavity geometry described in Ref. [13]. Figure 10 shows that synchrotron radiation has a much bigger impact than wakefields both on the emittance and on the induced energy spread. In particular, a counterintuitive result was obtained: In the presence of radiation, the wakefields slightly improve the beam quality during the deceleration.

The longitudinal phase space is shown in Fig. 11. It can be noted that, while none of the arcs is isochronous, their combined effects preserve the bunch length reducing the impact of the rf curvature. The beam parameters are summarized in Tables IV and V, respectively, at the IP and at the dump (after the deceleration). The beam is transported to the IP with an acceptable emittance growth. The impacts of the beam-beam interaction and SR in arc6 are evident but not detrimental to the deceleration. The beam envelope remains well within the aperture even at the end of the deceleration, as shown in Fig. 12.

It should be noted that the emittance blowup poses a lower limit to the injection or dump energy that is independent from the one due to the multibunch effects and can be more restrictive. Indeed, further deceleration of

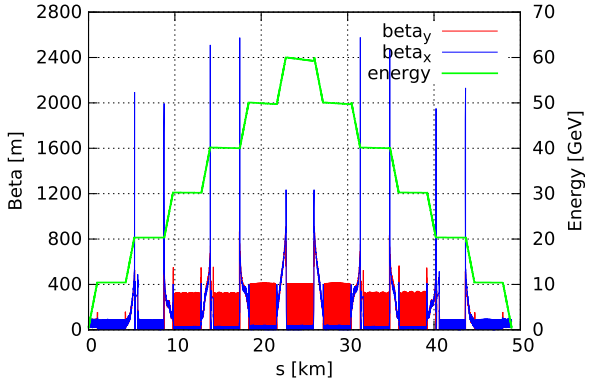


FIG. 9. Beta functions and energy profile obtained following a bunch throughout the entire LHeC lattice.

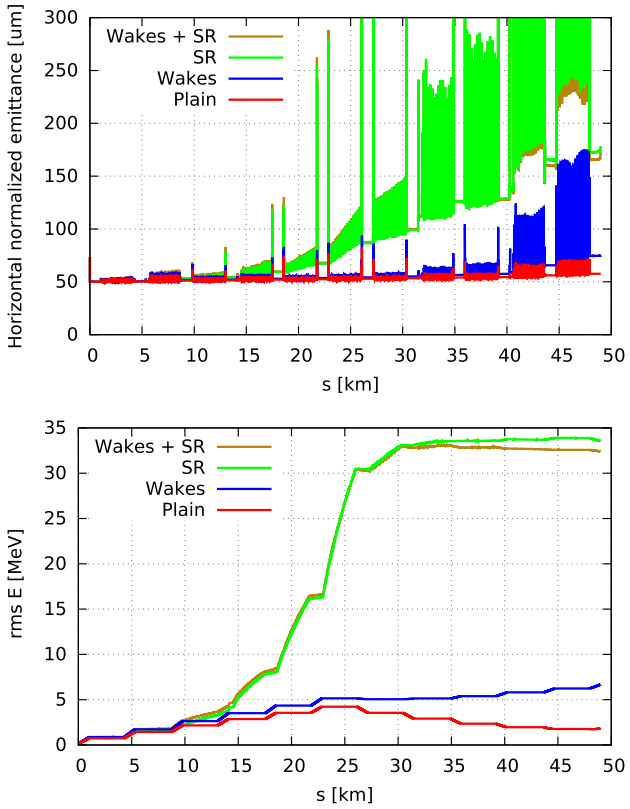


FIG. 10. Horizontal emittance and energy rms of a bunch tracked from the injector to the dump with an initial horizontal offset of 1 mm. The blowups caused by synchrotron radiation and wakefields are compared. The emittance includes the dispersion contribution; thus, its value in the arcs is not significant.

the beam yields losses of the tail particles. The maximum current would then be limited by the energy deposition causing material activation or damage and eventually quenching. Furthermore, the rf power requirements would increase for cavities where the losses start to take place as a consequence of degradation of the energy recovery process. Adding more quadrupole magnets in the linacs as proposed in Sec. II A would allow one to relax this limit, helping to reduce the injector energy and power consumption. An effective chromatic correction in the arcs and in the spreaders may as well be beneficial, resulting in a significant improvement of the overall machine cost and performance.

### B. Multibunch effects

PLACET2 allows one to simulate the machine operation with a continuous beam, by setting up a long train of bunches for tracking. It simultaneously propagates all the bunches, preserving their time sequence in each beam line. In this framework, multibunch effects can be computed realistically in the presence of multiturn recirculation. A model of the transverse long-range wakefields (LRWs) is currently implemented in PLACET2. LRWs take place when

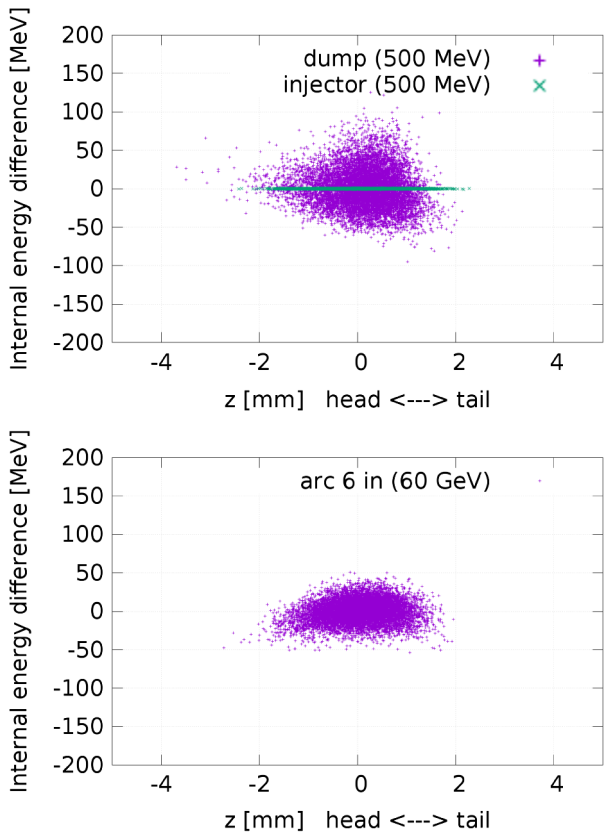


FIG. 11. Longitudinal phase space at the injection and at the dump (top) and at the IP (bottom).

a bunch passing through a cavity excites higher-order modes (HOMs). If their $Q$ values are big enough, the HOMs may persist, kicking the subsequent bunches. High current and strong HOMs can establish a positive feedback leading to beam breakup. The operation of the LHeC as a Higgs factory requires high currents, up to 150 mA in the linacs [4], which poses a concern for the beam stability.

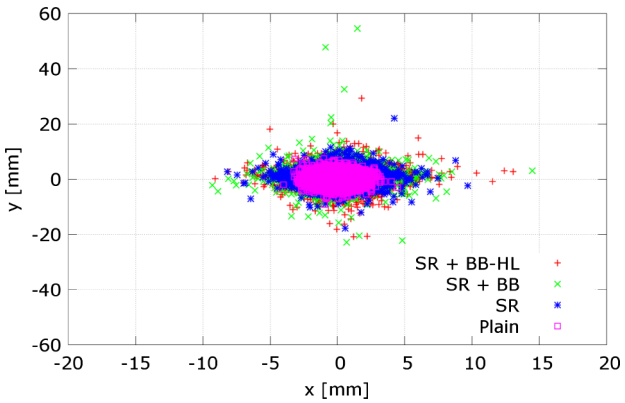


FIG. 12. Transverse beam profile at the end of the last linac, after the deceleration, including synchrotron radiation and beam-beam with standard and Higgs factory (high-luminosity) parameters. The beam contains 5000 macroparticles, and the initial distribution is Gaussian with no cuts.

TABLE IV. Initial beam parameters compared to the ones at the IP in the presence of synchrotron radiation.

| | Initial or CDR | IP |
|---|---|---|
| $\varepsilon_x$ [$\mu$m] | 50 | 57.4 |
| $\varepsilon_y$ [$\mu$m] | 50 | 50.8 |
| $\delta$ [%] | 0.20 | 0.026 |
| rms $x$ [$\mu$m] | 7.20 | 7.66 |
| rms $y$ [$\mu$m] | 7.20 | 7.21 |
| rms $z$ [mm] | 0.600 | 0.601 |
| rms $e$ [MeV] | 1.00 | 15.4 |

TABLE V. Beam parameters at the dump. The columns show the values for SR only, SR and beam-beam, and SR and beam-beam with the Higgs factory (high-luminosity) parameters.

| | Final SR | SR + BB | SR + BB-HL |
|---|---|---|---|
| $\varepsilon_x$ [$\mu m$] | 107 | 133 | 165 |
| $\varepsilon_y$ [$\mu$m] | 87 | 125 | 158 |
| $\delta$ [%] | 5.9 | 5.9 | 5.9 |
| rms $x$ [mm] | 1.52 | 1.67 | 1.86 |
| rms $x'$ [mrad] | 0.08 | 0.09 | 0.10 |
| rms $y$ [mm] | 2.42 | 3.03 | 3.15 |
| rms $y'$ [mrad] | 0.07 | 0.09 | 0.09 |
| rms $z$ [mm] | 0.66 | 0.66 | 0.66 |
| rms $e$ [MeV] | 29.7 | 29.5 | 29.6 |

For the multibunch simulation, the same setup as described in Sec. III A was used. The tracking was performed using single-particle bunches. The beam-beam computation GUINEA-PIG was substituted by an amplitude-dependent kick. The simplified beam-beam calculation overestimates the beam-beam effect, as in reality the electrons oscillate around the proton beam and receive a smaller kick. The HOMs considered are the transverse dipole modes of the superconducting proton linac cavity design, scaled to 802 MHz.

In order to evaluate the LRW impact, the machine is completely filled with approximately 6000 single-particle bunches perfectly aligned. One misaligned bunch is then injected, followed by many bunches again perfectly aligned. The perturbation introduced by the misaligned bunch is propagated to the others, as can be seen in Fig. 13. There are two important parameters: the slope of the tail, which determines whether and how fast the perturbation is damped, and the $F$ parameter that represents the total amplification of the beam action, defined as the squared sum of all the amplitudes [14]. This sum is convergent and mostly driven by the bunches that are close to the exciting one.

## IV. BUNCH RECOMBINATION PATTERN

The LHeC operation foresees continuous injection and multiturn recirculation. In this scenario, more bunches at

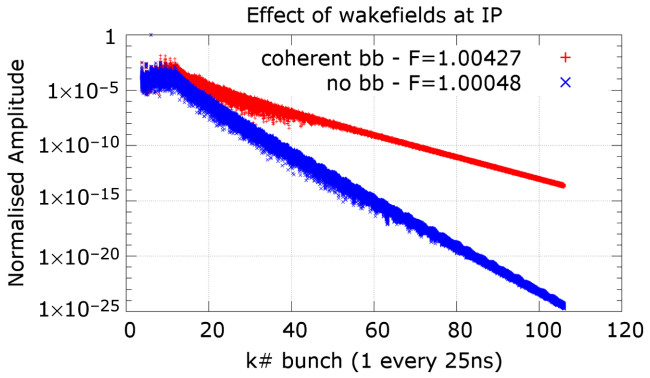


FIG. 13. Normalized actions of the bunches at the IP. Only the bunch with action 1 carries an initial misalignment. All other bunches are excited by LRWs. Each bunch contains $4 \times 10^9$ electrons.

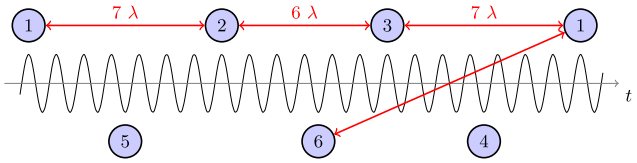


FIG. 14. When the recirculation is in place, the linacs are populated with bunches at different turns (the turn number is indicated).

different energies are interleaved in the linacs, appearing in periodic sequences. The spreader and recombiner designs, employing fixed-field dipoles, do not pose timing constraints. This gives us full control of the recombination pattern that can be selected by adjusting the length of the return arcs to the required integer number of $\lambda$.

A good choice for the recombination pattern consists of almost equal spacing (compatibly with the rf) of the bunches in the rf buckets. In order to minimize the bunch, cross talk is advantageous to maximize the separation between the bunches at the lowest energy: the ones at the first and sixth turns. This is illustrated in Fig. 14.

It has been verified that a pattern where bunches at the first and sixth turns closely follow each other reduces the beam break up threshold current.

## V. CONCLUSIONS AND OUTLOOK

Extensive tracking simulations have been performed for the LHeC ERL design. Using the newly developed code PLACET2, we completed a single-bunch end-to-end tracking and a multibunch simulation of the ERL operation. They allowed us to validate the beam dynamics, verifying the preservation of beam quality at the IP and the feasibility of beam deceleration to the dump. The beam-dynamics investigations cover the incoherent synchrotron radiation, beam-beam, and short- and long-range wakefields.

Following this study, a number of improvements have been made in the LHeC lattice, taking important steps towards its feasibility. Criteria for the multiturn linac optimization have been presented. Beam line sections such as the spreader and recombiner have been redesigned to reduce the impact of the synchrotron radiation while better containing the beta functions. The first design of the detector bypass has been completed. Realistic parameter tables for the rf compensating sections have been compiled. Finally, criteria for the bunch recombination pattern have been explained.

The next major steps of the LHeC study should aim at the integration of the interaction region, estimates of the beam gap required for the ion cleaning, and evaluations of tolerances in terms of the field quality and phase stability.

## ACKNOWLEDGMENTS

The authors thank Edward Niessen for his help with the GUINEA-PIG computations of the beam-beam effect.

[1] D. Pellegrini, A. Latina, and D. Schulte, PLACET2: a Novel Code for Beam Dynamics in Recirculating Machines, in *Proceedings of the 6th International Particle Accelerator Conference, IPAC-2015, Richmond, VA, 2015* (JACoW, Richmond, VA, 2015), MOPJE068.

[2] J. A. Fernandez *et al.*, A large Hadron electron collider at CERN: Report on the physics and design concepts for machine and detector, J. Phys. G **39**, 075001 (2012).

[3] F. Willeke, HERA hits new heights, *CERN Courier* **45**, 17 (2005).

[4] F. Zimmerman, O. Brüening, and M. Klein, The LHeC as a Higgs Boson Factory, in *Proceedings of the 4th International Particle Accelerator Conference, IPAC-2013, Shanghai, China, 2013* (JACoW, Shanghai, China, 2013), MOPWO054.

[5] A. Milanese, Warm magnets for LHeC/Test Facility arcs, in *Proceedings of the LHeC Workshop, 2014* (unpublished), https://indico.cern.ch/event/278903/session/6/contribution/41.

[6] O. Grobner, Vacuum Performance, in *Proceedings of the 3rd Workshop on LEP Performance, Chamonix, France, 1993*, edited by J. Pole (CERN, Geneva, Switzerland, 1993), p. 529, https://cds.cern.ch/record/248984.

[7] A. Zaltsman and R. Lambiase, High Power RF Systems for the BNL ERL Project, in *Proceedings of the 24th Particle Accelerator Conference, PAC-2011, New York, 2011* (IEEE, New York, 2011), TUP125.

[8] J. Schwinger, On radiation by Electrons in a Betatron, Report No. LBNL-39088, 1996, transcribed by M. A. Furman.

[9] F. Wittgenstein, A. Hervé, M. Feldmann, D. Luckey, and I. Vetlitsky, in *Proceedings of the 11th International Conference on Magnet Technology (MT-11)*, edited by T. Sekiguchi and S. Shimamoto, Construction of the L3 Magnet (Springer, Netherlands, 1990), pp. 130–135.

[10] D. Pellegrini, S. A. Bogacz, A. Latina, and D. Schulte, Single and Multi-bunch End-to-end Tracking in the LHeC, in *Proceedings of the 6th International Particle Accelerator Conference, IPAC-2015, Richmond, VA, 2015* (JACoW, Richmond, VA, 2015), MOPJE066.

[11] D. Schulte, Beam-Beam Simulations with Guinea-Pig, in *Proceedings of the ICAP98, Monterey, CA, 1998* (SLAC, Menlo Park, CA, 1998), http://cds.cern.ch/record/352676.

[12] K. Bane, Short-Range Dipole Wakefields in Accelerating Structures for the NLC, Report No. SLAC-PUB-9663, 2003.

[13] R. Calaga, A design for an 802 MHz ERL Cavity, Report No. CERN-ACC-NOTE-2015-0015, 2015.

[14] D. Schulte, Multi-Bunch Calculations in the CLIC Main Linac, in *Proceedings of the 23rd Particle Accelerator Conference, Vancouver, Canada, 2009* (IEEE, Piscataway, NJ, 2009), FR5RFP055.